DOE/BC/15211-3
(OSTI ID: 750286)

# A 2-D PORE-NETWORK MODEL OF THE DRYING OF SINGLE-COMPONENT LIQUIDS IN POROUS MEDIA

Topical Report
December 1999

By
Yanis C. Yortsos
A.G. Yiotis
A.K. Stubos
A.G. Boudouvis

Work Performed Under Contract No. DE-FG22-96BC14994/SUB
and Contract No. DE-AC26-99BC15211

University of Southern California
Los Angeles, California

**National Petroleum Technology Office**
**U. S. DEPARTMENT OF ENERGY**
**Tulsa, Oklahoma**

DOE/BC/15211-3
Distribution Category UC-122

# A 2-D Pore-Network Model of the Drying of Single-Component Liquids in Porous Media

By
Yanis C. Yortsos
A.G. Yiotis
A.K. Stubos
A.G. Boudouvis

January 2000

Work Performed Under Contract No. DE-AC26-99BC15211

Prepared for
U.S. Department of Energy
Assistant Secretary for Fossil Energy

Thomas B. Reid, Project Manager
National Petroleum Technology Office
P.O. Box 3628
Tulsa, OK 74101

University of Southern California
Petroleum Engineering Program
Department of Chemical Engineering
Los Angeles, CA 90089-1211

## Table of Contents



### Figures

## Tables

## Abstract

The drying of liquid-saturated porous media is typically approached using macroscopic continuum models involving phenomenological coefficients. Insight on these coefficients can be obtained by a more fundamental study at the pore- and pore-network levels. In this paper, we present a model based on a pore-network representation of porous media that accounts for various processes at the pore-scale. These include mass transfer by advection and diffusion in the gas phase, viscous flow in liquid and gas phases and capillary effects at the gas-liquid menisci in the pore throats. We consider isothermal drying in a rectilinear horizontal geometry, with no-flow conditions in all but one boundary, at which a purge gas is injected at a constant rate. The problem is characterized by two dimensionless parameters, a diffusion-based capillary number, *Ca*, and a Peclet number, *Pe*, in addition to the various geometrical parameters of the pore network. Results on the evolution of the liquid saturation, the trapped liquid islands and the drying rate are obtained as a function of time and the dimensionless parameters. The importance of trapped liquid islands on screening mass transfer to the continuous liquid cluster is emphasized. For fixed parameter values, the drying front does not in general obey invasion percolation rules. However, as drying progresses, and depending on the relative magnitude of the capillary and Peclet numbers, a transition to a percolation-controlled problem occurs. Effects of capillarity and mass transfer on saturation profiles and drying rates are discussed. The results are then used to discuss upscaling to continuum models.

# Introduction

Drying of porous solids is a subject of significant scientific and technological interest in a number of industrial applications including coatings, food, paper, textile, wood, ceramics, building materials, granular materials, electronic devices and pharmaceuticals (Pan *et al.*[14]; Bruin and Luyben[1]; Simpson[22,23]; Panagiotou *et al.*[15]; Fortes and Okos[5]; Chen and Pei[3]). In a different context, drying in porous media is involved in distillation and vaporization processes associated with soil remediation (Ho and Udell[7]) as well as in the recovery of volatile hydrocarbons from oil reservoirs by gas injection (Le Gallo *et al.*[11]).

Generally, in drying, a single- or multi-component liquid phase gradually evaporates and is removed from the complex porous structure via combined heat and mass transfer processes. The traditional description relies on phenomenological approaches, in which the porous medium is a continuum, the dependent variables, like moisture content, are volume-averaged quantities and the relation of fluxes to gradients is through empirical coefficients (van Brakel[26]; Waananen *et al.*[27]). Such approaches essentially ignore the effect of the pore microstructure which is of key importance for a quantitative understanding of the process. In fact, drying involves many pore-scale mechanisms, for example the motion of individual gas-liquid menisci residing in the pore space, diffusion in the gas phase (for a single-component liquid) and the liquid phase (for a multi-component liquid), viscous flow in both phases, capillarity and possibly liquid flow through connected films, all of which need to be accounted for. We should note that although it also involves the receding of liquid-vapor interfaces, drying is not a typical external displacement process, like external drainage, which has been well studied in the past. Rather similarities exist to processes like solution gas drive and/or boiling in porous media, where the displacement of the liquid phase is driven internally by mass or heat transfer and which have been only recently investigated (Li and Yortsos[12], Satik and Yortsos[20]).

The physical context of the problem considered here is schematically depicted in Fig. 1, which shows an exaggerated schematic of a fractured network. Liquid is trapped in the matrix and may vaporize as a result of an injected purge gas flowing primarily in the fractures. The actual overall problem is quite complex, requiring the consideration of the network of fractures and the matrix continuum, gas flow and mass transfer in the fracture

network and the multi-dimensional mass transfer from the matrix continuum to the fracture network. For simplicity, we will consider the much simpler geometry of the pore-network model shown in Fig. 1b, which involves a 2-D rectangular matrix block, all but one boundaries of which are impermeable to flow and mass transfer. We will also neglect gravity. Extension to 3-D geometries is in principle straightforward, although computationally costly, while equally feasible is the consideration of gravity effects. We consider isothermal conditions, under the assumption that heat transfer in the solid operates much faster than mass transfer in the gas phase. Finally, a single-component liquid phase is aasumed. It is of note that this approach applies also to the vaporization of trapped NAPL's in low-permeability layers or regions (as in Ho and Udell[7]).

At any time during the process, evaporation of the liquid leads to the receding of the liquid (drying) front, leaving behind disconnected clusters of liquid and liquid films (in corners of capillaries, or as thin films), the size and location of which change continuously with time. In general, four different spatial regions can be identified[25] (Fig. 1c):

(i) a far-field (from the fracture) region consisting of the initial liquid;

(ii) a region where both liquid and gas phases are macroscopically connected (this region is absent in 2-D square pore-networks as the present, however);

(iii) a region where the liquid phase is disconnected and consists of individual clusters of variable sizes (trapped islands of liquid); and

(iv) a near-field (to the fracture) region consisting primarily of the connected gas, with the liquid phase in the form of pendular rings, corner films or thin films on the solid surface, the thickness of which is progressively reduced towards a "totally dry" regime.

Evidently, the gas phase is macroscopically continuous in the last three regimes. On the basis of his experiments, Shaw[21] has postulated that liquid films may also provide hydraulic conductivity to the liquid phase in these regimes.

The conventional approach to modeling drying is based on a continuum description, the simplest model for which involves only the two limiting regions (the far-field and the near-field), separated by a planar drying front. The latter recedes due to diffusion-controlled mass transfer obeying a square-root time dependence. Recently, Tsimpanogiannis *et al.*[25] proposed a more complex 1-D model using transverse-averages. Their model involves

various coefficients, which need to be evaluated from a pore-network study, however (see also Stubos and Poulou[24]). Tsimpanogiannis *et al.*[25] also developed a theory based on pore-scale considerations, for the description of the scaling properties of the drying front. Specifically, they showed that consideration of viscous effects makes drying equivalent to Invasion Percolation in a Stabilizing Gradient (IPSG) (e.g. see Xu *et al.*[28]). Liquid flow in the porous matrix driven by capillary pressure gradients (the so-called capillary pumping effect) and the allowance of film flow is an essential element of that theory. Based on the fact that drying is controlled by diffusion, in contrast to external drainage which is controlled by the injection rate, a power law relation of the evaporating front width with a modified, diffusion-based capillary number was obtained and shown to be compatible with the experimental data of Shaw[21]. However, other important features of the process, including the partition of the liquid phase in various regimes, the mass transfer rates, etc., were not explored.

Following recent trends in describing processes in porous media, several studies in recent years used a pore-network approach to model drying. Key to these approaches is the consideration of mass transfer, elements of which were described by Li and Yortsos[12] and Jia *et al.*[8], among others. Various pore-network models with specific applications to drying were proposed originally by Nowicki *et al.*[13], and more recently in a series of papers by Prat and co-workers (Prat[17]; Laurindo and Prat[9,10]; Prat and Bouleux[18]). In parallel, Pot *et al.*[15] used lattice-gas automata to simulate evaporation in a 2-D lattice. Nowicki *et al.*[13] presented a numerical simulation of the process at the pore-network level. However, the authors did not expand on the particular patterns and regimes obtained or on the associated effects on drying rates. Prat's studies represent the first attempt to characterize theoretically drying patterns and their rate of change in porous structures. Prat[15] studied the formation of drying patterns assuming capillary control, neglecting viscous effects and considering mass transfer only by quasi-static diffusion. Laurindo and Prat[10] provided a macroscopic assessment of the importance of liquid films. Based on percolation patterns and isothermal conditions, they computed drying rates by solving a quasi-static diffusion equation in the gas phase. Prat and Bouleux[18] focused on diffusional mass transfer and the effect of gravity on the front structure. In earlier experiments using horizontal glass-bead packs (Shaw[21]), viscous forces were found to be important for explaining the formation of an evaporating front (separating

continuous liquid from gas) of a finite size. More generally, we expect that advection and viscous effects will have an impact on patterns and drying rates. Existing pore-network models address slow drying, controlled by capillarity and/or gravity and by diffusion, ignoring advection and/or viscous effects. We note that consideration of advection in the gas phase requires knowledge of the pressure field, which is coupled to viscous flow in the two phases and capillary effects. Thus, these two processes must be treated simultaneously.

The present paper is motivated by the above lack of completeness and attempts to shed light to mass transfer and/or viscous effects on the development of drying patterns. It is also motivated by the need to provide reliable coefficients in the appropriate continuum models, and in a sense it represents a continuation of the work by Tsimpanogiannis *et al.*[25], except that film flows are ignored. We consider the isothermal drying (at room temperature) of a porous block, initially saturated with liquid (hexane), subject to flow of air in the fracture and in the absence of gravity. The paper is organized as follows: First, we present details of the pore-network approach. The various mechanisms described previously (diffusion in gas phase, viscous flow in both phases, capillarity) are addressed. Then, simulation results are obtained for the drying patterns and rates, for various values of the dimensionless parameters governing the process. The latter involve a mass transfer-based capillary number and the Peclet number based on the gas velocity in the fracture. The results are subsequently analyzed using simpler statistical theories, such as Invasion Percolation (IP). Various limiting cases are identified and analyzed. In particular, we pay attention to the trapped islands surrounding the drying front, which due to their screening effect on mass transfer play an important role in the problem. Scale-up issues as well as effects of various parameters not considered in the pore network are discussed in the last section.

## Formulation

The physics that govern the process under consideration are as follows. Isothermal conditions are assumed, heat diffusion in the solid being faster than mass diffusion in the gas. This assumption will certainly not apply in the case of poorly conducting solids, however. The 2-D pore network is horizontal, thus gravity effects, which could be

dominant, depending on the magnitude of the gravity Bond number[18], are not included. These can be readily implemented in the pore-network simulation. However, gravity can mask important mass transfer effects, while the understanding of the simpler drying process in its absence, is still incomplete, as noted above. Here, drying is driven by the flow of a purge gas (air) in the fracture. Liquid evaporates at the gas-liquid interface at rates determined by mass transfer in the gas phase, governed by advection and diffusion. The temperature is sufficiently far from the boiling point of the liquid, so that evaporation rates are diffusion-controlled and the binary mixture in the gas phase can be assumed to be dilute.

In general, during the process, the liquid resides in two different regions (Fig. 1c): a "continuous" cluster (CC), which is part of the initial liquid cluster and can be defined as being "sample-spanning" across the two lateral edges of the matrix block; and various "disconnected" clusters (DC), which have become disconnected from the CC and from one another, and they are not "sample spanning" (see below). Their geometry, size, configuration and location are important to drying patterns and rates. Liquid may also reside in films (thicker corner films or thin films) in gas-occupied pores, that may provide hydraulic continuity between clusters and/or with the fracture. These are not considered here, although in all likelihood, they have non-trivial effects on drying patterns and rates, as will be discussed below. Receding of the liquid-gas interface in the various clusters occurs when the capillary pressure across a meniscus first exceeds the capillary threshold at the pore where the meniscus resides. Accounting for capillarity requires the consideration of pressure fields in the liquid and gas phases. Flow in the latter is assumed to be slow and viscous-controlled.

In the pore-network formulation, the porous medium is represented using a standard pore-network approximation in terms of pore bodies (here spheres) and pore throats (here cylinders) arranged in a lattice[2,4]. For the 2-D simulations below, a square lattice is used. Pore bodies contain most of the volume, throats provide resistance to flow and transport, as well as capillary pressure thresholds. For drying applications, we can further distinguish three types of pore bodies: Those fully occupied by gas (belonging to the gas phase and denoted by G), those fully occupied by liquid (belonging to the liquid phase and denoted by L) and those at the gas-liquid interface (in which a meniscus resides, denoted by I). The latter may be further subdivided in completely empty (CE) and partly empty (PE) pores[25]

(see below). As noted above, this classification does not account for corner films. In the simulations, pore body and throat radii were uniformly distributed in the range 0.37-0.74 mm and 0.16-0.32 mm respectively. The lattice length $\ell$ (pore center to pore center) was taken to be 2 mm. The fracture was also represented as a pore network (here a 1-D chain), with pore and throat radii taken equal to 0.77 mm and 0.275 mm, respectively. We must point out that this fracture representation may not necessarily apply to a real problem, where larger sizes should be expected, but it was taken here for convenience of the sensitivity analysis to follow.

Mass transfer of the vapor in the gas phase obeys the convection-diffusion equation

$$\frac{\partial C}{\partial t} + \boldsymbol{u} \cdot \nabla C = D \nabla^2 C \tag{1}$$

where $C$ is the vapor concentration, $\boldsymbol{u}$ is the gas-phase velocity and $D$ is the diffusion coefficient. In a G or I pore surrounded by G pores, this is further discretized as

$$(1.0 - S_i) V_i \frac{\Delta C_i}{\Delta t} = \sum_j \left[ D \pi r_{ij}^2 \frac{C_i - C_j}{\ell} \right] + \sum_j \left[ \frac{\pi r_{ij}^4 (P_i - P_j)}{8 \mu \ell} \overline{C_{ij}} \right] \tag{2}$$

where $S_i$ is the gas saturation at pore i, $V_i$ is the volume of pore i, $\Delta C_i$ is the change in $C_i$ during the elapsed time $\Delta t$, $r_{ij}$ is the radius of the throat connecting pores i and j, $\mu$ is the gas viscosity, $P$ is the pressure and $C$ is the concentration at the pore. Note that the advection term is upstream weighted, namely

$$\overline{C}_{ij} = C_i \qquad \text{if } P_i > P_j, \quad \text{and} \quad \overline{C}_{ij} = C_j \qquad \text{if } P_j > P_i$$

The pressure fields are obtained from a separate computation to be discussed below. We note the use of a simplified Poiseuille-type approximation for the flow across two adjacent sites, and the assumption that mass transfer between the sites is by diffusion and convection (namely, dispersion in a single pore is not considered). However, mass transfer between two

adjacent sites, one of which resides in the fracture, is enhanced by considering a velocity-dependent mass transfer coefficient[19]

$$\left(\frac{K_f \ell}{D}\right) = 1 + Pe^a \tag{3}$$

where the Peclet number, $Pe$, is defined as

$$Pe = \left(V_f \frac{\ell}{D}\right) \tag{4}$$

$a$ is an exponent, and $V_f$ is the linear gas velocity through the fracture. When a neighboring site contains a meniscus (PE), its concentration is the vapor equilibrium concentration. The boundary conditions for mass transfer involve zero flux at the lateral boundaries, a constant volumetric flux at the entrance of the fracture and zero concentration at the entrance and exit of the fracture. The latter could be modified to a zero-concentration gradient condition, but this was not considered.

The single-component liquid in the liquid phase and the non-condensible gas in the gas phase satisfy continuity equations. For their calculation, we solve for the pressure fields in G and L sites. Fluxes between adjacent sites of the same type are computed by Poiseuille-law type flow resistances, where the viscosity is considered constant

$$Q_{ij} = \left(\frac{P_i - P_j}{\ell}\right) \frac{\pi r_{ij}^4}{8\mu} \tag{5}$$

$$\sum_j Q_{ij} = 0 \tag{6}$$

The flux between an I site and a G (or an L) site depends on the status of the I site. We need to distinguish two types: If the capillary pressure of the meniscus in site I is not large enough for it to penetrate an adjacent throat, the meniscus remains stationary, resulting in zero flow in that direction. Then, in this site we assign only a gas pressure value and zero

mass flux rates of gas or liquid across the meniscus. This site was denoted as a CE pore[25]. In the next time step, the meniscus may be subject to a sufficiently high capillary pressure that can lead to the subsequent penetration of an adjacent pore and liquid displacement. Then, the site becomes partly empty (PE). For simplicity, we will assume that in such pores the capillary pressure is zero (equal pressures of liquid and gas). This is certainly another simplification of the real problem, which is much more complex, involving a variable capillary pressure within PE pores. In I sites, conservation of mass of the evaporating liquid gives the liquid velocity $u_{\ell n}$ at the interface as a function of the rate of emptying of the site and the diffusive flux in the gas phase, namely[25]

$$-D\frac{\partial C}{\partial n} = \varrho_\ell (u_{\ell n} - u_n) \tag{7}$$

where $D$ is the diffusion coefficient, $\varrho_\ell$ is the mass density of the liquid, $u_n$ is the velocity of the front and $n$ denotes the normal to the interface. Likewise, conservation of mass of the non-condensible gas leads to[25]

$$u_n = u_{gn} \tag{8}$$

where $u_{gn}$ is the gas velocity at the meniscus. These were used as interface conditions coupling the flow fields in the two phases. We note that the above treatment of mass transfer applies in the dilute limit. In the case of non-dilute mixtures, counter-diffusion in the gas phase needs to be considered as well.

Updating of interfaces and marching in time proceeds as follows. At any given time, sites have the designation, G, L or I, and pressure and concentration fields are known. The L sites can be part of the original liquid cluster (CC) or they belong to disconnected finite-size clusters (DC), which become trapped through the evaporation process. In the subsequent time step, the overall rate of evaporation from each of the liquid clusters is evaluated. Pressure fields are calculated and PE pores of type I are emptied according to the appropriate mass balances. The time step is selected such that it equals the minimum time required to empty completely any of the available PE sites. If at the current time, no PE

pores are available to any (or all) of the clusters (namely all I pores are of the CE type) the throat with the smallest capillary threshold in the perimeter of any given cluster is the next throat to be invaded, at which time, the corresponding invaded site becomes an I site of the PE type. To determine this throat the liquid pressure is uniformly lowered inside the cluster, until the capillary pressure exceeds for the first time the smallest capillary threshold. Equivalently, this can be obtained by invading the throat with the smallest difference between the gas pressure in the site and the corresponding capillary pressure threshold of the throat. Implicit to the above is the absence of hydraulic continuity between disconnected clusters, namely the absence of liquid films. Nonetheless, invasion must occur, since due to evaporation there is a continuous loss of mass from the liquid clusters. At the conclusion of the time step, concentration fields in the gas phase are computed and the process continues. This algorithm is essentially the same one used by Li and Yortsos[12] and Satik and Yortsos[20] in the related problems of phase change by solution gas-drive or boiling. All calculations are done explicitly in time. Pressure fields are computed using Successive Over-Relaxation, while concentration fields are obtained from (2) in a straightforward manner.

From a dimensional analysis of the problem, there are three main dimensionless groups: (i) a diffusion-based capillary number $Ca$ defined as

$$Ca = D\mu_\ell C_{\ell e}/\gamma^\ell \varrho_\ell \tag{9}$$

where $\mu_\ell$ is the viscosity of the liquid phase and $C_{\ell e}$ is the equilibrium concentration, expressing the ratio of viscous to capillary forces, based on a diffusion-driven velocity; (ii) a Peclet number, $Pe$, defined by (4), expressing the ratio of advection to diffusion in the gas phase, based on the linear velocity assuming only flow in the fracture; and (iii) the viscosity ratio, $M$, between liquid and gas viscosities. The latter is typically large and will not be considered in the sensitivity analysis to follow. We point out that one may also define a capillary number based on the fracture velocity. Clearly, the latter would control high-rate processes at early stages, while the diffusion-based capillary number controls the process at later times. These two capillary numbers are linearly related through the Peclet number, thus only two of these parameters are linearly independent. capillary number. In the presence of gravity, an additional dimensionless number, the Bond number

$$B = \frac{g(\varrho_l - \varrho_g)k}{\gamma} \tag{10}$$

expressing the ratio of gravity to viscous forces, must also be considered, where $k$ is the permeability of the porous medium. Geometric parameters include the number of sites in the linear direction $N=L/l$, where $l$ is the typical pore length, the aspect ratio between mean pore size and pore length, as well as between mean pore size and mean throat size, a scaled variance of the size distribution, and the aspect ratio of the matrix block (here taken equal to 1). In this study, all geometric parameters are taken fixed, the aspect ratio of the matrix block is equal to 1, and emphasis is placed on the effect of the capillary and Peclet numbers. The effect of $N$ will be addressed in the discussion on scale-up.

## Results

A number of runs were conducted to simulate drying of liquid hexane in a matrix block of size 50x50. The corresponding physical parameter values are shown in Table 1.

*Table 1: Values of physical properties used.*

| | |
|---|---|
| Volumetric gas flow rates | 0.0-1.0$cm^3$/sec |
| Surface Tension | 19dyn/cm |
| Diffusion Coefficient | 0.0638$cm^2$/s |
| Equilibrium concentration | 2.66*$10^{-4}$gr/$cm^3$ |
| Liquid phase viscosity | 2.85*$10^{-3}$dyn*s/$cm^2$ |
| Gas phase viscosity | 1.71*$10^{-4}$dyn*s/$cm^2$ |
| Liquid phase density | 0.650gr/$cm^3$ |
| Gas phase density | 4.4*$10^{-3}$gr/$cm^3$ |

To carry out a sensitivity study, we varied the injection rate in the fracture, the interfacial tension and the diffusion coefficient. Table 2 shows the set of runs conducted.

*Table 2: Set of simulation runs.*

| Run | $Q$ ($cm^3/s$) | $\gamma$ (dyn/cm) | $D$ ($cm^2/s$) | $a$ | $Ca$ | $Pe$ | $t^*$ (s) |
|---|---|---|---|---|---|---|---|
| 1 | 1.00 | 19 | 0.0635 | 0.33 | $1.68*10^{6}$ | 1325 | 14238 |
| 2 | 0.45 | 19 | 0.0635 | 0.33 | $1.68*10^{-6}$ | 596 | 17983 |
| 3 | 0.25 | 1.9 | 0.0635 | 0.33 | $1.68*10^{-5}$ | 331 | 21340 |
| 4 | 0.25 | 19 | 0.0635 | 0.33 | $1.68*10^{-6}$ | 331 | 21340 |
| 5 | 0.25 | 60 | 0.0635 | 0.33 | $5.33*10^{-7}$ | 331 | 21340 |
| 6 | 0.25 | 100 | 0.0635 | 0.33 | $3.20*10^{-7}$ | 331 | 21340 |
| 7 | 0.25 | 19 | 0.0635 | 1.00 | $1.68*10^{-6}$ | 331 | 500 |
| 8 | 0.25 | 19 | 0.6350 | 0.33 | $1.68*10^{-5}$ | 33 | 4002 |
| 9 | 0.20 | 19 | 0.0635 | 0.33 | $1.68*10^{-6}$ | 265 | 22742 |
| 10 | 0.10 | 19 | 0.0635 | 0.33 | $1.68*10^{-6}$ | 132 | 27645 |
| 11 | 0.05 | 1.9 | 0.0635 | 0.33 | $1.68*10^{-5}$ | 66 | 33325 |
| 12 | 0.05 | 19 | 0.0635 | 0.33 | $1.68*10^{-6}$ | 66 | 33325 |
| 13 | 0.015 | 19 | 0.0635 | 0.33 | $1.68*10^{-6}$ | 19 | 45611 |
| 14 | 0.005 | 19 | 0.0635 | 0.33 | $1.68*10^{-6}$ | 6.7 | 57819 |
| 15 | 0.0005 | 19 | 0.0635 | 0.33 | $1.68*10^{-6}$ | 0.66 | 88752 |
| 16 | 0.0 | 19 | 0.0635 | 0.33 | $1.68*10^{-6}$ | 0.0 | 166132 |

The characteristic time $t^*$ denotes the time at which the matrix block empties at the maximum drying rate (which occurs at the first time step at which all liquid-gas interfaces are at the fracture-matrix boundary) and it is used to non-dimensionalize time. All simulations correspond to a fixed realization of the pore network, which, however, allows to study the sensitivity of drying patterns and rates to the other parameters. The development of ensemble-averaged drying curves is in progress. Results on drying patterns, concentration profiles, transversely-averaged saturation profiles and drying rates were obtained. We note that in order to demonstrate strong advection effects, the values of the Peclet number used in certain runs in the above table are high (perhaps unrealistically high).

We will use run 2 and run 15 to illustrate typical features from the simulation. These runs are typical of two limiting regimes, one in which capillary forces are dominant and mass transfer occurs by diffusion, and another in which viscous forces dominate and mass transfer is by advection. In addition, we will discuss a case (run 12) involving capillary

control in the phase partition, but advection control in mass transfer. As schematically depicted in Fig. 1c, the results show that the liquid phase consists of a main cluster (CC) and a number of discontinuous (DC) clusters at the perimeter of the CC (see Figs 2 and 3 for runs 2 and 15, respectively). These result from trapping of the liquid as the gas invades the liquid-occupied region. The patterns of the CC and/or the DCs depend on the value of the capillary pressure across the perimeter of each of these clusters as follows.

If viscous forces are not sufficiently strong across a given cluster (for example, as in run 15, Fig. 3), the capillary pressure variation is negligible, and the cluster takes the pattern of Invasion Percolation (IP), in which the next throat to be invaded by the gas is that with the smallest capillary threshold (here, the one with the largest size) among all perimeter throats of that cluster. This condition depends on the value of the capillary number, the rates of drying (which also set viscous pressure gradients[25]) and the size of the cluster. Under otherwise similar conditions, small DCs are more likely to follow an IP pattern. A detailed check of the sequence of invasion showed that run 15 followed IP rules at any time during the process, while run 2 did not. Patterns corresponding to IP and diffusion-only mass transfer were obtained in run 16, where $Pe=0$. The corresponding saturation patterns are shown in Fig. 4. Comparison with Figs. 2 and 3 shows substantial differences in the patterns between runs 2 and 15 (or 16) and some difference (at early times) between runs 15 and 16. The latter reflects mass transfer effects, due to the different Peclet numbers in the two runs.

Because of their relevance to real problems and the fact that capillary-dominated patterns eventually appear as late-time regimes, we provide here some additional discussion of their properties. We first recall that all simulations in this paper were conducted assuming the absence of film flows, thus DCs are hydraulically disconnected from each other and the CC. Under these conditions, in a capillary-controlled pattern (such as run 15 and 16), while each cluster obeys locally IP rules, the sequence of penetration is dictated by the mass transfer rates across the perimeter of each cluster. In the related study of Li and Yortsos[12] this process was termed *local percolation*. Clusters closer to the open boundary are subject to a faster evaporation, compared to those further away, and are emptied faster. The end result is the development of gradients in the size of the isolated liquid clusters, with clusters

closer to the fracture having smaller size (see also below). These gradients reflect mass transfer, rather than viscous effects. Nonetheless, the pattern of the CC is still dictated by IP rules. Clearly, however, the overall pattern would be a function of the drying rates, namely of the value of the *Pe*. We must note that under this regime of local percolation, different clusters may have different-size throats being invaded at the same time. In other words, it is possible that the drying of a given DC occurs by the emptying of a throat *i*, which is smaller than the largest perimeter throat, *j*, of another cluster, which due to negligible mass transfer is not being invaded (of course, as a result of capillary control, throat *i* is the largest among all perimeter throats of the first cluster).

The above analysis of capillary-controlled patterns is based on the assumption of negligible film flow. If, on the other hand, hydraulic continuity exists among all clusters (for example through liquid films) then, in the small *Ca* limit, the next throat to be penetrated will be the throat with the smallest threshold among *all* perimeter throats of *all* clusters. In the liquid-to-gas phase change study of Li and Yortsos[12], this was termed *global percolation.* In the absence of viscous or gravity gradients, such a process could lead to a deep penetrating front of a fractal nature, and liquid saturation gradients will not develop, in the sense that the proximity of a particular front site to the open boundary cannot influence the time at which it is invaded. Gradients in saturation will develop in the case of the viscous-capillary-gravity competition. This regime was implied in many previous studies, including the work of Tsimpanogiannis et al.[25]. Because of the qualitative differences, it is evident that establishing hydraulic continuity is an important role played by liquid films and needs to be further explored.

In the limit when capillarity is negligible (as in run 2), the pattern deviates substantially from IP and almost follows a piston-like displacement (PD) (Fig. 2). Under these conditions, the capillary resistance of a throat is negligible, and the pattern is exclusively determined by mass transfer considerations, much like in the dissolution of a solid. The rate of generation of DCs and their size are smaller and the liquid phase consists mostly of a CC. Such conditions are not likely to persist for a long time in the typical case, however, where late-time drying patterns are likely to be of the IP type. We need to add that when viscous forces in the gas phase are important in setting the pattern (as is the case in

run 2, for example), the receding of the CC has some of the properties of IPSG in a fracture-matrix system (Haghighi *et al.*[6]). In such cases, the higher capillary pressure upstream leads to a preferential invasion in the matrix in the upstream direction, thus leading to patterns that appear to be slanted (from the upstream to the downstream direction) as shown in run 2 (Fig. 2).

Regardless of the magnitude of the capillary forces, the presence of discontinuous clusters is very significant in the development of the pattern. These clusters result in the screening of a part of the CC from the fracture, hence from the region of high concentration gradients, and lead to a balanced rate of drying among the two types of clusters, through the following stabilizing feedback mechanism. For example, if the mass transfer rates from the CC are too large, they will result in a faster rate of consumption of the CC, leading to the generation of a larger number of DCs, which in turn screen the CC from further mass transfer and slow down its rate of drying. Conversely, if the rate of drying of the CC is too small, most of the reduction in liquid saturation occurs from the DCs, the size and number of which decrease, leading to an increased mass transfer and a subsequent increased rate of consumption of the CC. It follows that for fixed values of the capillary and Peclet numbers, the statistics of the DCs, namely their number density and size distribution, remain approximately constant. In particular, the region where the DCs reside (which we may denote as the front region) is approximately of a constant width (Figs. 2-4). We should mention that similar findings were observed by Prat and Bouleux[18], although in the different situation where the gradients are provided by gravity rather than mass transfer. The size of the frontal region can be estimated using arguments from Invasion Percolation with Trapping (IPT) as described in the Appendix.

The screening of the CC from the region of high mass transfer is evident in the concentration profiles (Figs. 5-6). Depending on the value of the Peclet number and the location of the front, the concentration field in the gas phase may or may not be sensitive to the detailed structure near the front. For small values of the Peclet number (as in run 15, Fig. 5), the process is almost diffusion-controlled and the concentration resembles the much smoother concentration field surrounding an effective continuum (as also found by Li and Yortsos[12]). This despite the rather complex geometry of the front (see Fig. 3), which is rather complex (and in fact, fractal). Almost identical patterns were obtained for run 16 and

they are not shown. As advection increases and at early times, however, the region of concentration gradients is a narrow boundary layer surrounding the front. At later times (panel 3 in Fig. 6), this is not uniformly developed, as poorly accessible regions cannot be effectively probed by the flow field. This mass transfer effect is also evident in the simulations of run 12 (Fig. 7). This run has a Peclet number almost two orders of magnitude larger than in run 15, although the sequence of the liquid patterns is almost identical (and is not shown here for simplicity). However, because of the much stronger advection effects, concentration profiles are much steeper in most places in run 12, resulting in proportionally higher drying rates (Fig. 7). At the same time, the effect is non-uniform spatially, and there exist regions in which diffusion is controlling. Strong advection effects similar to these were also reported in a related problem of bubble growth driven by heat transfer[20].

Runs 2 and 15 are typical of the two limiting regimes and can be analyzed in a relatively straightforward fashion. Intermediate patterns are more difficult to analyze, as they have features from both regimes. When both capillarity and viscous forces compete, the receding of the drying front does not follow strictly IP or PD rules. Depending on the rates of evaporation as well as the size of the individual clusters, there may exist more than one pore of the PE type at the same time, and these pores may not necessarily correspond to the IP or the PD sequence. We must point out that Tsimpanogiannis *et al.*[25] the spatial extent over which the front follows IP rules was estimated using scaling arguments, from which the following relation was developed for 3-D patterns

$$\sigma_{fr} \approx \left( \frac{2\Sigma X_{fr}}{Ca} \right)^{0.47} \tag{11}$$

where $\sigma_{fr}$, $X_{fr}$, $\Sigma$ are non-dimensionalised front width, frontal position and variance of the pore size distribution, respectively. Implicit to this relation was the assumption of global percolation (namely of hydraulic continuity via film flow). This result is not expected to hold here. Nonetheless, clusters of small size will erode following local IP rules. In larger-size clusters, however, the spatial extent over which IP rules apply would be limited. Thus, the problem acquires some of the characteristics of IPSG[25]. As time increases, drying rates

decrease, as the front recedes further away, and the width of the front, where IP is exhibited, increases accordingly. One expects that after sufficiently long time, the process will approach a state where IP applies for all clusters. Some arguments from IPT are furnished in the Appendix to estimate the size of the front in this problem.

A typical case in which viscous and capillary forces compete is run 4, shown in Figs. 8-9. The invasion pattern belongs to neither of the two limiting regimes. There is evidence of IPSG in the matrix, similar to run 2, but also a multiple number of DCs, similar to run 15. The concentration profiles for this run (Fig. 9) are similar to those of run 12, and suggest substantial concentration gradients in boundary layer regions near the front. At the same time, regions far from the fracture are effectively being screened, despite the large Peclet number in this run, leading to mass transfer similar to the diffusion-controlled case (run 15).

In macroscopic continuum models a quantity of interest is the transverse-averaged saturation profiles. Results for runs 15, 12, 2 and 4 are shown in Figs. 10-13, respectively, for four different values of the fraction of the liquid volume occupying the matrix (and which corresponds to the four panels of the previous figures). As expected, runs 15 and 12 have almost identical profiles (Figs. 10-11), their patterns being dictated by IP rules, even though their mass transfer characteristics are not the same. Differences due to the latter are reflected in their drying rates to be discussed below. Gradients in saturation develop, due to the continuous receding of the front. As discussed above and in the Appendix, these gradients reflect the screening of inaccessible, deeper-lying parts of the liquid front from high concentration gradients, the resulting limited mass transfer, and the development of a frontal region of finite width (which is constant in the absence of viscous effects, but increases with time in their presence). The profiles in runs 2 and 4 (Figs. 12-13) reflect a more uniform penetration, at early times, due to the preferential receding of the liquid in the upstream direction as a result of strong viscous effects. These are not unlike the profiles in the drainage of a matrix block[6]. As time increases, however, all profiles eventually approach a state which progressively becomes capillary- and diffusion-controlled.

Fig. 14 shows drying curves for the various runs simulated. As discussed, the time was made dimensionless with the time $t^*$ it would take to empty the matrix block under conditions of the maximum rate. It then follows that the slope of the drying curves is the

dimensionless rate of drying (relative to the maximum drying rate). Note that because the maximum rate depends on the Peclet number in the fracture (roughly as $Pe^{1/3}$) this plot emphasizes processes under convection control and should be interpreted with care, as far as the upscaling of the process is concerned. The figure shows clearly the existence of a Constant-Rate-Period (CRP), followed by a period of continuously declining rates. From an analysis of the patterns, we have found that the CRP lasts roughly until the time when the CC has lost continuity with the fracture. This is in agreement with indirect experimental findings from tests on chalk samples initially containing liquid pentane and dried by methane injection along the fracture[11]. In addition, macroscopic arguments set forth by Stubos and Poulou[24] on the basis of the same experimental data have led to the same conclusion. Indeed, as long as the liquid is continuously connected to the fracture, the combination of enhanced evaporation rate (through the coefficient given by (3)) and capillary gradients leads to a constant drying rate. This is evident when considering the low Peclet number run 15 or the IP run 16 in Fig. 14 where the CRP is very short due to the fast receding of the liquid phase from the fracture. A close examination of the drying curves shows that the highest rate and the longest CRP are found in run 4. In this "critical" case the gas pressure developing close to the entrance of the fracture is high enough to cause the breaking of menisci in the left side of the matrix block. On the contrary, this cannot happen on the right side sustaining for relatively large times sufficient liquid contact with the fracture (see patterns in Fig. 8). Thus the constant rate during the CRP reflects the detailed mass transfer characteristics during the process and is realization-dependent. By increasing the interfacial tension value in run 4 (runs 5 and 6 of Table 2), we find that the drying rate and the CRP drop to levels similar to the ones determined for the low Peclet number cases (Fig. 15). In fact, the gas pressure is not any more sufficient to overcome the capillary thresholds and the case resembles more and more to IP. When $\gamma$ decreases on the other hand (run 3), all menisci in contact with the fracture break at early times and the CRP is very short. The drying rate also drops accordingly (Fig. 15). For the case of IP-controlled processes, the end of the CRP in terms of the amount of liquid left can be readily estimated from the analysis in the Appendix.

## Discussion

The above analysis was based on a number of simplifying assumptions, most of which were made to illustrate various effects. We single out the small size of the fracture pores and throats taken, in order to allow for a study of the viscous-capillary competition at the rates considered. At a larger contrast of fracture/matrix capillary and permeability characteristics, the onset of a PD regime will be delayed as far as the flow rate is concerned. We also note that the Peclet number in some of the runs can be considered unrealistically high. Such simulations were purposedly made to exaggerate the effect of advection in mass transfer. In general, flow rate-driven effects will dominate the process at early times, and particularly during the CRP, which will be controlled, as a result, by the detailed geometry and process characteristics. It is in this regime and time period, where pore-network simulations, such as these, can have a significant impact. At later stages, the front recedes, viscous effects and advective mass transfer become less important and the process becomes capillary- and diffusion-controlled. In this regime, the analysis discussed in the Appendix applies and various results from the theory of Invasion Percolation with Trapping can be used to describe the process.

A key simplification made in the paper concerns the absence of liquid films. As discussed, these can be important in providing hydraulic continuity between clusters, which can drastically alter the patterns and the location and size of the DCs and the CC. Work in this direction, in particular in the incorporation of film flows in the pore-network simulation, is currently under way. At present, their effect is difficult to assess. We also need to mention the restriction to single-component liquids, which eventually leads to the complete evaporation of the liquid clusters. In the presence of a non-volatile component, the disconnected liquid clusters will not disappear, but will affect adversely the mass transfer rates. Such effects need to be considered as well.

The results can be used for upscaling to macroscopic continuum models. Following the CRP, where the process becomes capillary- and diffusion-controlled, the theory of IPT discussed in the Appendix can be used to elucidate the distribution of the liquid phase, and the size and extent of the DC region. This information can then be utilized to construct model diffusion problems, the solution of which can be implemented in the calculation of

needed coefficients in macroscopic models (for example, as required in Tsimpanogiannis *et al.* [25] ). Such work is also under way. On the other hand, the CRP is not necessarily amenable to such a statistical theory description, given that non-local effects of rate and viscous forces (or finite-size effects in the case of capillary control) are important. The solution of this problem must be sought by conducting extensive pore-network simulations, including the ensemble-averaging of results over many realizations, something that was not done here.

## Conclusions

In this paper we presented a pore-network model for the drying of a single-component liquid in porous media. The model accounts for various processes at the pore-scale including mass transfer by advection and diffusion in the gas phase, viscous flow in liquid and gas phases and capillary effects at the gas-liquid menisci in the pore network. A 2-D version of the model under isothermal conditions in a rectilinear horizontal geometry was formulated. Drying is driven by the flow of a purge gas is injected at a constant rate. The problem is characterized by two dimensionless parameters, a diffusion-based capillary number, $Ca$, and a Peclet number, $Pe$, in addition to the various geometrical parameters of the pore network. Results on the evolution of the liquid saturation, the trapped liquid islands and the drying rate were obtained as a function of time and the dimensionless parameters. In the absence of liquid film flow, the importance of trapped liquid islands in screening mass transfer to the continuous liquid cluster was emphasized. This results in saturation gradients, and the development of patterns which are different than in the case of flow continuity between the different clusters. For fixed parameter values, the drying front does not in general obey invasion percolation rules. However, as drying progresses, and depending on the relative magnitude of the capillary and Peclet numbers, a transition to a percolation-controlled problem occurs. In fact, it is likely that such is the case in many realistic situations. Effects of capillarity and mass transfer on saturation profiles and drying rates were discussed. The results provide insight on the process. The pore network simulation can

also be used to provide expressions for various coefficients in macroscopic continuum models, currently treated empirically. Work in this direction is in progress.

## Acknowledgements

The research of one of the authors (YCY) was partly supported by DOE contract DE-AC2699BC15211, the contribution of which is gratefully acknowledged. Partial funding by the JOULE Programme of the European Commission is also acknowledged (Contract JOF3-CT95-0008). We acknowledge useful discussions with S. Poulou and I.N. Tsimpanogiannis.

## References

[1] Bruin, S., Luyben, K.C.A.M., *Advances in Drying*, **1** (1980) 155.

[2] Chandler, R., Koplik, J., Lerman, K., Willensen, J. F, *J. Fluid Mech.*, **119** (1982) 249.

[3] Chen, P., Pei, D.C.T., *Int. J. Heat Mass Transfer*, **32** (1989) 297.

[4] Fatt, I., *Trans. AIME*, **207** (1956) 144.

[5] Fortes, M., Okos, M. R., *Advances in Drying*, **1** (1980) 119.

[6] Haghigi, M., Xu. B., Yortsos, Y.C., *J. Coll. Interf. Sci*, **166** (1994) 168.

[7] Ho, C. K., Udell, K.S., *Int J. Heat Mass Transfer*, **38** (1995) 339.

[8] Jia, C., Shing, K., Yortsos, Y.C., *J. Contam. Hydrol.*, **35** (1999) 363.

[9] Laurindo, J. B. & Prat, M., *Chem. Eng. Sci.*, **51** (1996) 5171.

[10] Laurindo, J. B. & Prat, M., *Chem. Eng. Sci.*, **53** (1998) 2257.

[11] Le Gallo, Y., Le Romancer, J. F., Bourbiaux, B., Fernades, G., paper SPE 38924 (1997).

[12] Li, X. & Yortsos, Y. C., *Chem. Eng. Sci.*, **50** (1995) 1247.

[13] Nowicki, S. C., Davis, H. T., Scriven, L. E., *Drying Tech.*, **10** (1992) 925.

[14] Pan, S. X., Davis, H. T., Scriven, L. E., *Tappi Journal*, **78** (1995) 127.

[15] Panagiotou, N. M., Stubos, A. K., Bamopoulos, G., Maroulis, Z. B., *Drying Tech.*, **17** (1999) 2107.

[16] Pot, V., Appert, C., Melayah, A., Rothman, D. H., Zaleski, S., *J. Phys. II*, **6** (1996) 1517.

[17] Prat, M., *Int. J. Multiphase Flow*, **21** (1995) 875.

[18] Prat, M., Bouleux, *Phys. Rev. E*, **60** (1999) 5647.

[19] Quintard, M. & Whitaker, S., *Adv. Water Res.*, **17** (1994) 221.

[20] Satik, C. & Yortsos, Y. C., *J. Heat Trans.*, **118** (1995) 455.

[21] Shaw, T. M, *Phys. Rev. Lett.*, **59** (1987) 1671.

[22] Simpson, W. T., *Drying Tech.*, **2** (1983) 235.

[23] Simpson, W. T., *Drying Tech.*, **3** (1984) 353.

[24] Stubos, A. K. & Poulou, S., paper SPE 56415 (1999).

[25] Tsimpanogiannis, I. N., Yortsos, Y. C., Poulou, S., Kanellopoulos, N., Stubos, A. K., *Phys. Rev. E.*, **59** (1999) 4353.

[26] van Brakel, J., *Advances in Drying*, **1** (1980) 212.

[27] Waananen, K. M., Litchfield, J. B., Okos, M. R., *Drying Tech*, **11** (1993) 1.

[28] Xu, B., Yortsos, Y.C., Salin, D., *Phys. Rev. E*, **57** (1998), 739.

## Nomenclature

*Roman Letters*

| | |
|---|---|
| $B$ | Bond number |
| $C$ | concentration, gr/cm$^3$ |
| $C_{te}$ | equilibrium concentration, gr/cm$^3$ |
| $Ca$ | Capillary number |
| $D$ | diffusion coefficient, cm$^2$/s |
| $g$ | gravity acceleration, cm/s$^2$ |
| $k$ | permeability, cm$^2$ |
| $K_f$ | mass transfer coefficient along the fracture, cm/s |
| $\ell$ | distance between pore centers, cm |
| $p$ | percolation probability of the invading phase |

$p_c$ critical percolation probability of the invading phase
$P$ pressure, dyn/cm$^2$
$Pe$ Peclet number
$q$ percolation probability of the defending phase
$q_c$ critical percolation probability of the defending phase
$Q$ flow rate, cm$^3$/s
$r$ radius, cm
$S$ gas saturation
$t$ time, s
$t^*$ time required for the liquid to evaporate at the maximum rate, s
$u_{\ell n}$ liquid velocity, cm/s
$u_{gn}$ gas velocity, cm/s
$u_n$ velocity of the interface, cm/s
$V_f$ gas velocity through the fracture, cm/s

*Greek letters*

$\gamma$ interfacial tension, dyn/cm
$\mu$ viscosity of the gas phase, dyn*s/cm$^2$
$\varrho_g$ density of the gas phase, gr/cm$^3$
$\varrho_\ell$ density of the liquid phase, gr/cm$^3$
$\sigma_{ft}$ non-dimensionalised front width
$\Sigma$ variance of the pore size distribution
$X_{ft}$ non-dimensionalised frontal position

# APPENDIX

Discontinuous clusters form as the perimeter of the CC recedes, due to gas invasion, and the receding phase becomes trapped. In the absence of mass transfer considerations and under capillary control, this is the well-known mechanism of Invasion Percolation with Trapping. In the latter, the statistics of the trapped clusters can be determined from knowledge of the percolation probability, $q$, at which the defending phase (here the liquid) is being invaded. In the particular process under consideration, the invasion of the CC is a drainage process in which the invading (gas) phase percolation probability is near its percolation threshold

$$p \sim p_c \ (=1/2 \text{ for a 2-D square lattice})$$

Then, the defending phase is at percolation probability $q=1-p \sim 1-p_c$. Knowledge of $q$ allows one to estimate various statistics of the disconnected, trapped clusters, since the latter can be accurately approximated by the finite-size clusters of a mixed site-bond percolation process at percolation probability $q$. For example, the size of the largest DC follows the percolation scaling

$$\xi \sim |q-(1-p_c)|^{-\nu}$$

where $\nu$ is the correlation length exponent. Statistics are also available (or can be obtained) for other properties of these finite-size clusters. In the above, it is implicitly assumed that $p_c < 1/2$, and that $\xi << N$. When the latter condition fails, as is the case in the simulations here, where $p_c = 1/2$, the largest (cut-off) size is set by the width of the lattice $N$. The above analysis can be used to estimate the statistics of screened DCs around the front, which are not subject to substantial drying rates, although not of the DCs at the frontier with the gas phase, which are being exposed to strong concentration gradients and a time-varying size.

In the presence of viscous effects, the invasion process is similar to IPSG, in which, in the absence of mass transfer effects, the largest size of the DCs is set by the Bond number of the process, namely

$$\xi \sim B^{-\frac{\nu}{\nu+1}}$$

In drying, an equivalent Bond number can be defined as follows[25]

$$B = \frac{Ca}{2\Sigma X_{ft}}$$

However, the incorporation of an IPSG theory in the trapping problem is yet to be done. In general, we expect that such a theory would lead to the result that the average size of the DCs becomes smaller as viscous forces increase, as is the case with the problem without trapping[25], and also as shown in the simulations.

We also conjecture that the same length scale, namely the average size of the largest DC, is also the scale for the width of the frontal region, namely the region containing the trapped clusters (DC). Indeed, as we argued in the main text, the mass transfer screening from the DCs sets the balance between them and the CC. We expect that at least for diffusion-controlled problems, this screening will be effectively set by the distance between DCs, which are all sources of constant concentration. Given that the only characteristic length in the problem is the average size of the DCs completes the argument in support of this conjecture.

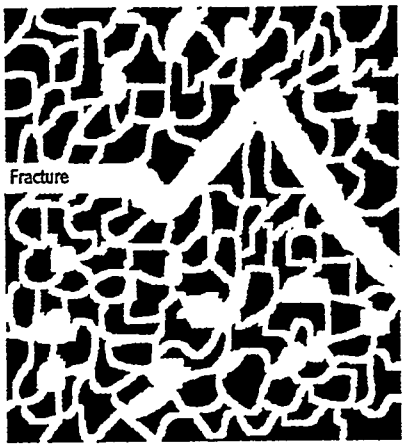


**Figure 1a** Schematic representation of fractured porous media.

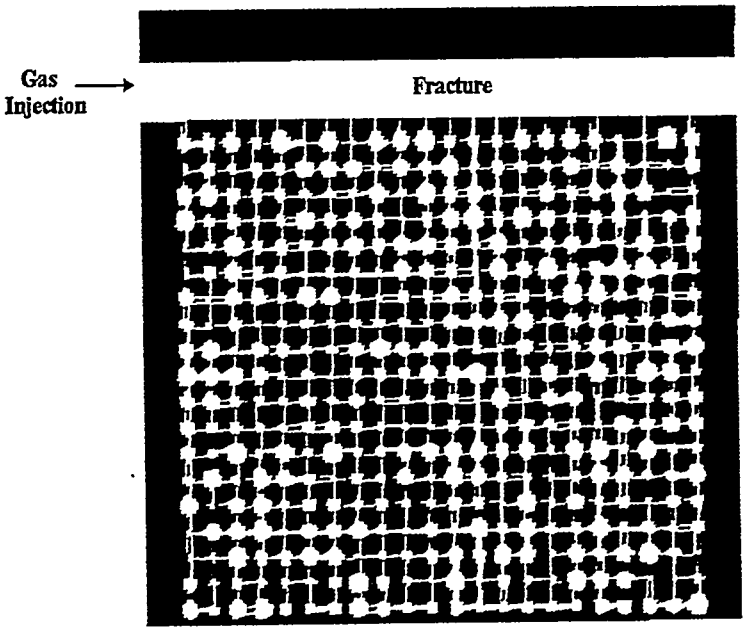


**Figure 1b** Pore-network model representation.

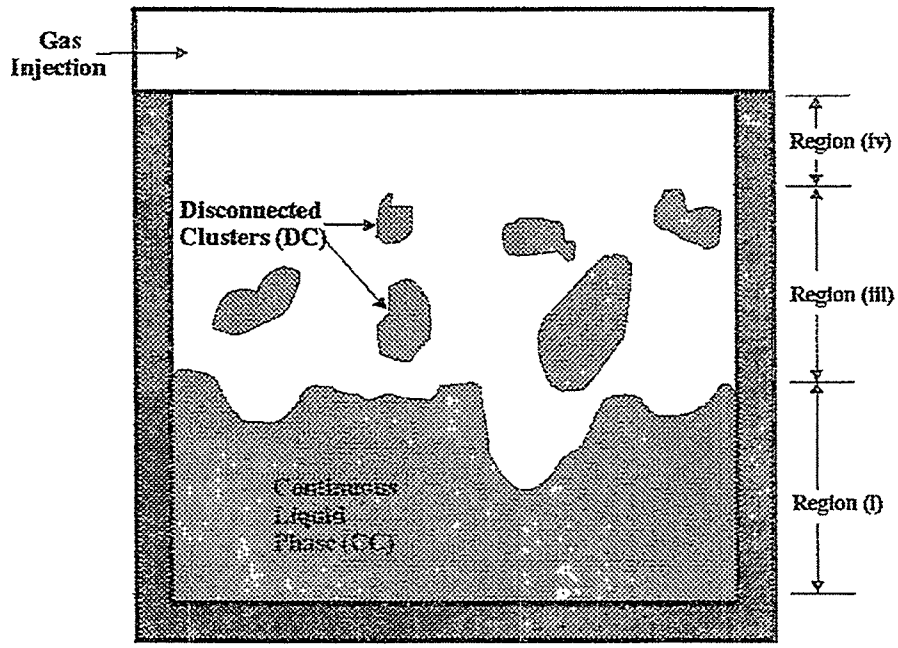


**Figure 1c** Classification of typical saturation pattern.

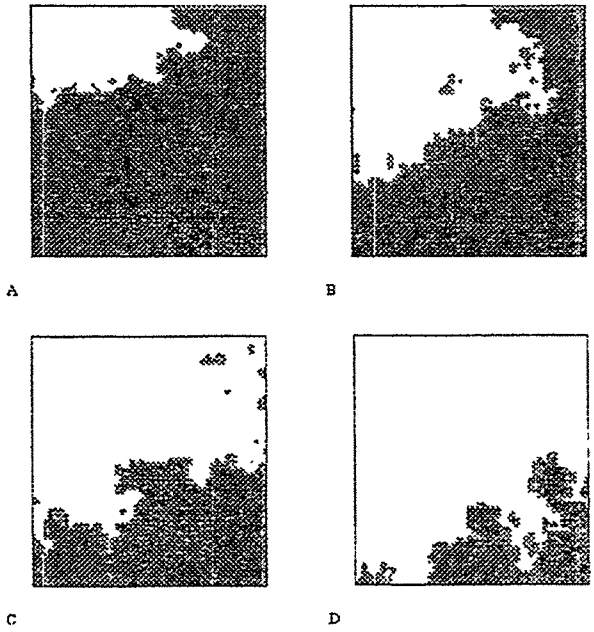


**Figure 2** Phase distribution patterns for run 2 at four different liquid fractions corresponding to 20%, 40%, 60% and 80%. The liquid phase is black and the gas phase is white

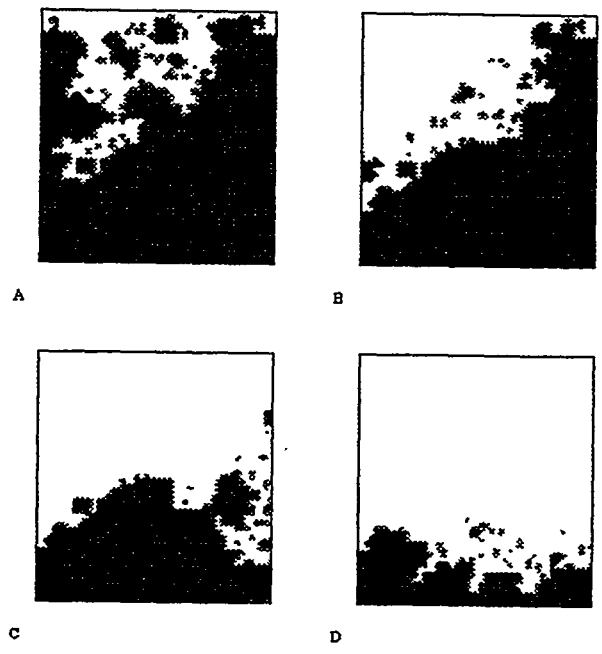


**Figure 3** Phase distribution patterns for run 15 at four different liquid fractions corresponding to 20%, 40%, 60% and 80%. The liquid phase is black and the gas phase is white.

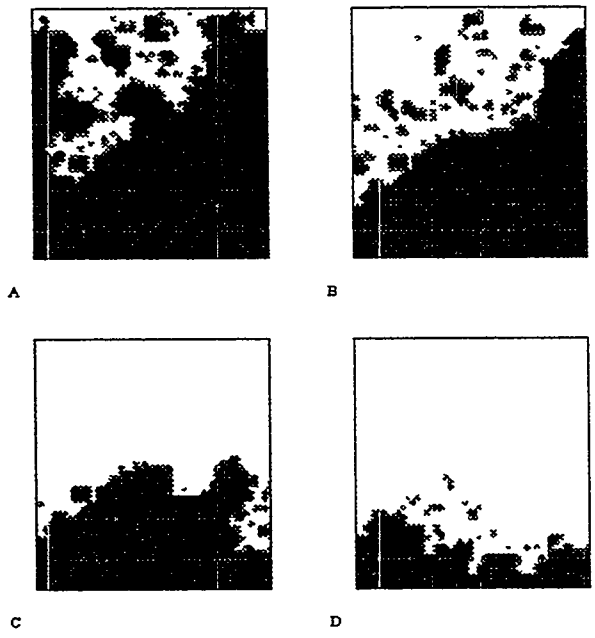


**Figure 4** Phase distribution patterns for run 16 at four different liquid fractions corresponding to 20%, 40%, 60% and 80%. The liquid phase is black and the gas phase is white.

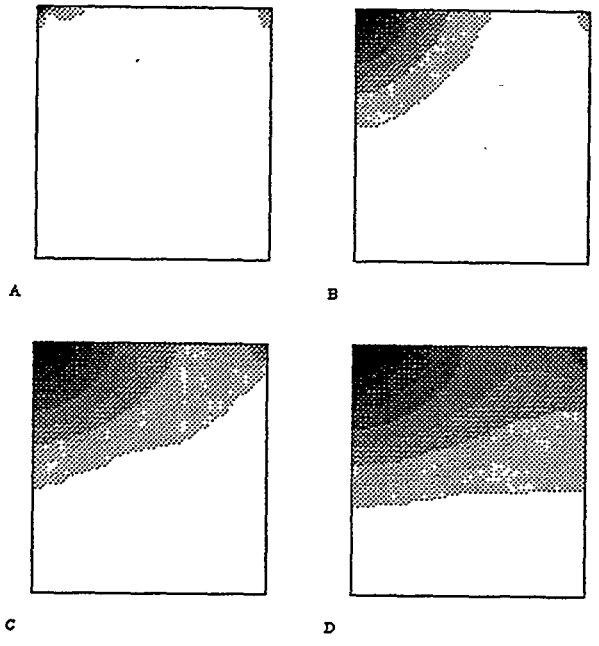


**Figure 5** Concentration patterns for run 15 at the four different occupation fractions. Darker colors indicate smaller concentrations.

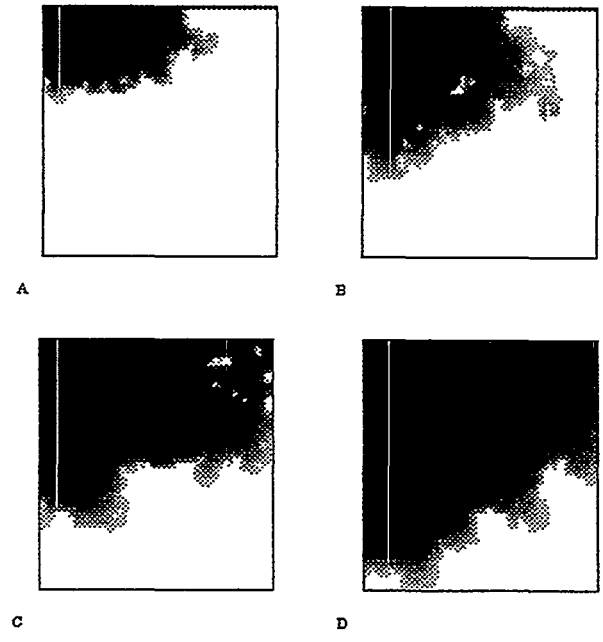


**Figure 6** Concentration patterns for run 2 at the four different occupation fractions. Darker colors indicate smaller concentrations.

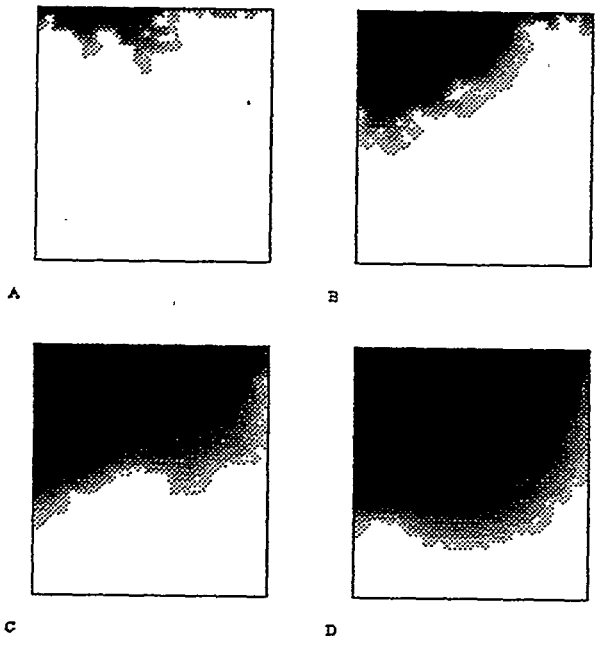


**Figure 7** Concentration patterns for run 12 at the four different occupation fractions. Darker colors indicate smaller concentrations.

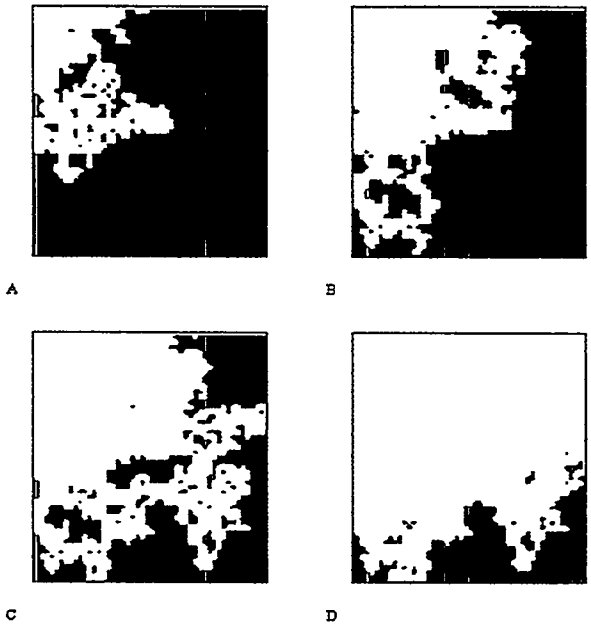


**Figure 8** Phase distribution patterns for run 4 at four different liquid fractions corresponding to 20%, 40%, 60% and 80%. The liquid phase is black and the gas phase is white.


**Figure 9** Concentration patterns for run 4 at the four different occupation fractions. Darker colors indicate smaller concentrations.

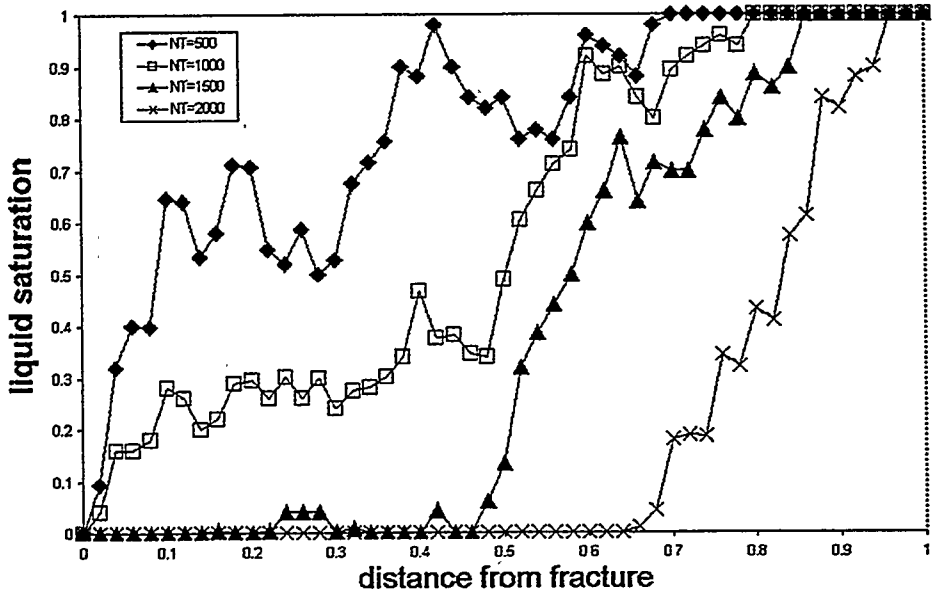


**Figure 10** Transversely-averaged saturation profiles for run 15.

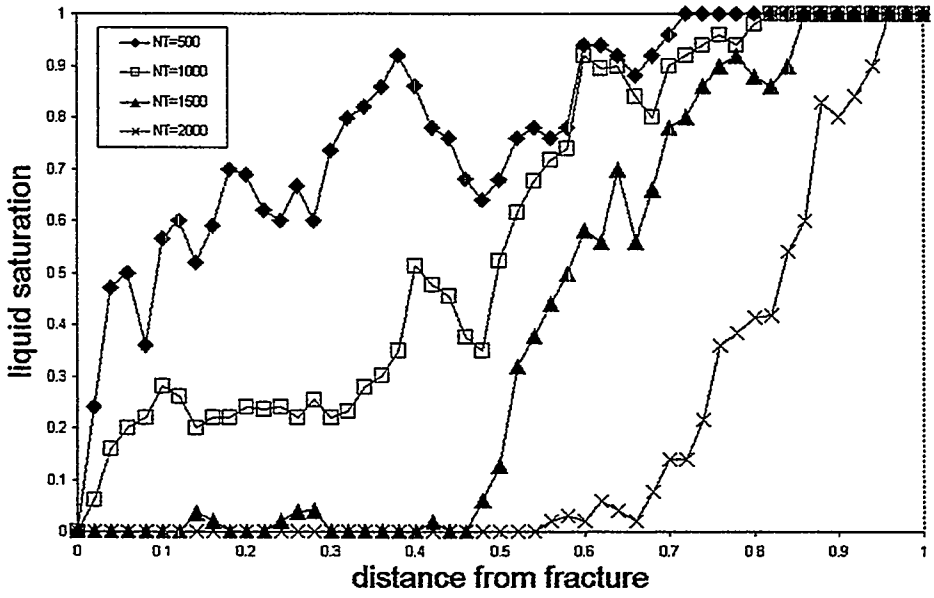


**Figure 11** Transversely-averaged saturation profiles for run 12.

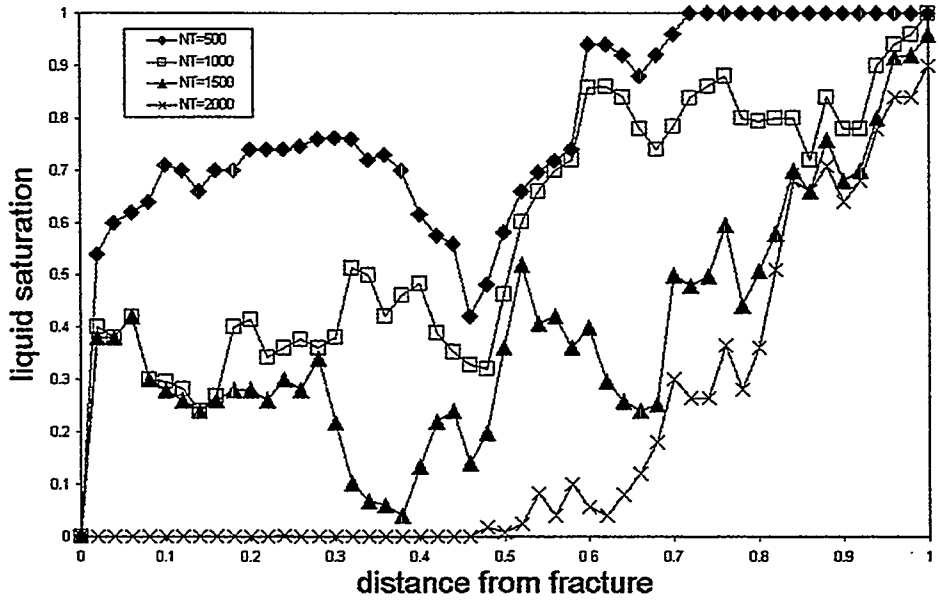


**Figure 12** Transversely-averaged saturation profiles for run 4.

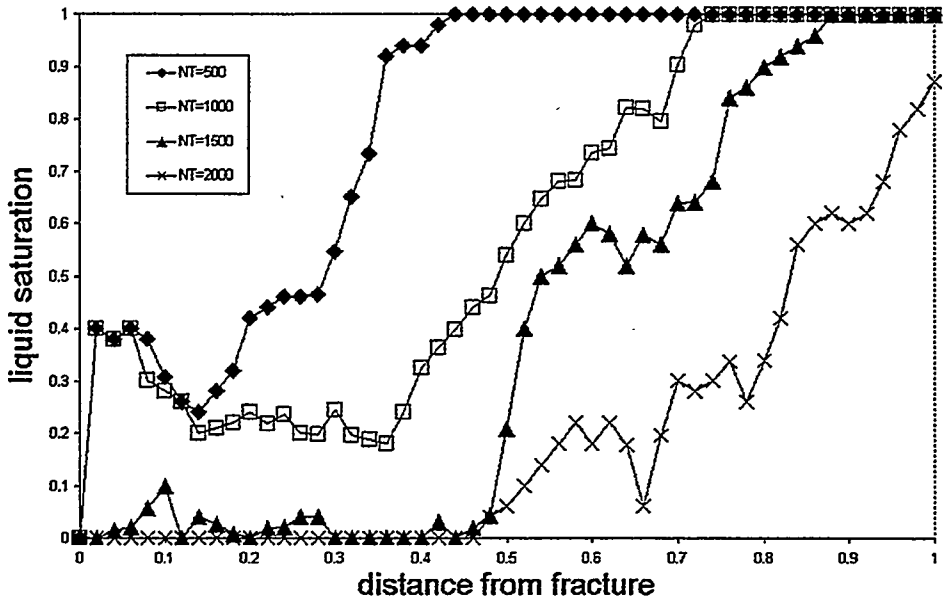


**Figure 13** Transversely-averaged saturation profiles for run 2.

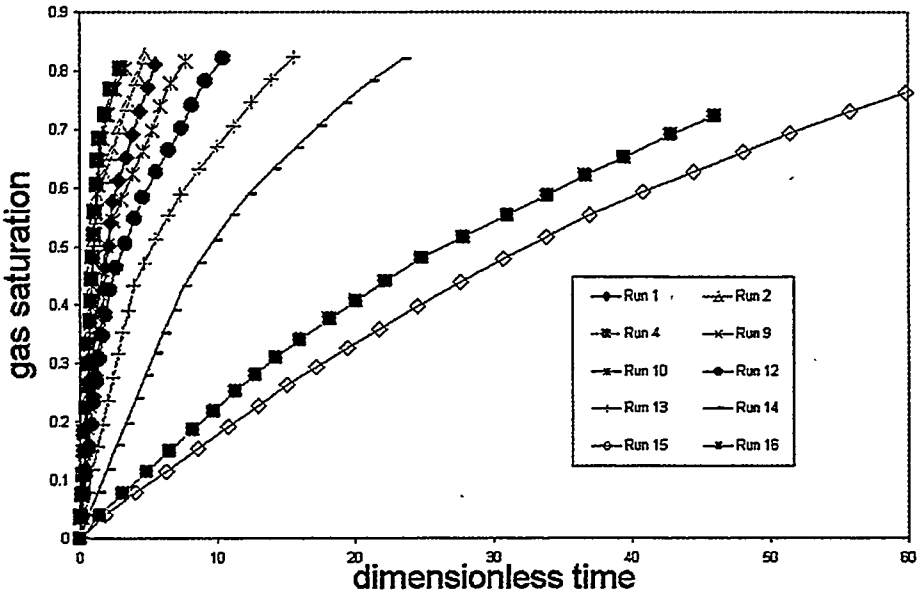


**Figure 14** Drying curves (gas volume fraction vs. dimensionless time) for various runs.

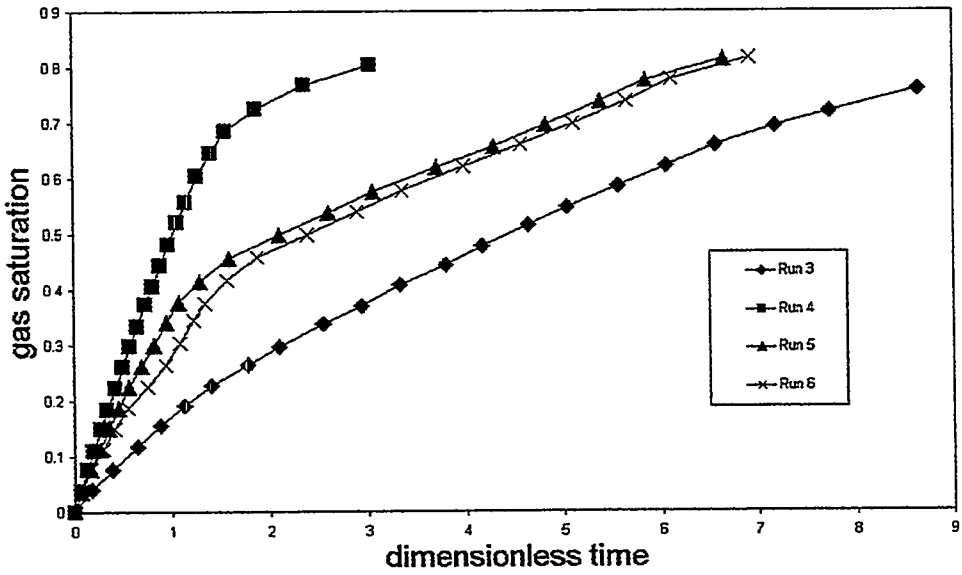


**Figure 15** Drying curves (gas volume fraction vs. dimensionless time) for runs 3-6.